Fuel 235 (2019) 350–362

Contents lists available at ScienceDirect

Fuel

journal homepage: www.elsevier.com/locate/fuel

Full Length Article

The distillation curve and sooting propensity of a typical jet fuel

Chiara Saggese[a], Ajay V. Singh[a], Xin Xue[b], Carson Chu[c], Mohammad Reza Kholghy[c,1], Tongfeng Zhang[c], Joaquin Camacho[a,2], Jennifer Giaccai[d], J. Houston Miller[d], Murray J. Thomson[c], Chih-Jen Sung[b], Hai Wang[a,*]

[a] Mechanical Engineering Department, Stanford University, Stanford, CA 94305, USA
[b] Department of Mechanical Engineering, University of Connecticut, Storrs, CT 06269, USA
[c] Department of Mechanical and Industrial Engineering, University of Toronto, Toronto, Canada
[d] Department of Chemistry, The George Washington University, Washington, DC 20052, USA

ARTICLE INFO

Keywords:
Jet fuel
Flame
Soot
Particle size distribution
Distillation curve

ABSTRACT

Real jet fuels are complex mixtures of many organic components, some of which are aromatic compounds. Towards the high-temperature end of the distillation curve, some of the fuel components are multi-ring compounds. A small amount of these high molecular weight species in the fuel could impact soot nucleation in practical engines especially when the fuel is injected as a spray. This work aims to highlight the variation of the sooting propensity of jet fuels as a function of distillate fractions and to examine the validity of a surrogate fuel in emulating soot production from real fuels. Particle size distribution functions and soot volume fractions are studied in a series of laminar premixed stretch-stabilized ethylene flames doped with Jet A, its various distillate fractions, and the 2nd generation MURI surrogate. Soot formation as a result of doping real jet fuel and its distillate fractions is also investigated in counterflow and coflow diffusion flames. The results show that the higher-boiling distillates mostly influence soot nucleation and produce substantially more soot in nucleation controlled flames than the light molecular fraction and jet fuel as received, while such an effect is seen to be small in flames where soot production is controlled by surface growth. The potential impact of distillate fractions on soot nucleation propensities is discussed.

1. Introduction

Conventional jet fuels are of a distillate origin of crude oils and multicomponent in nature. A typical jet fuel may contain thousands of hydrocarbon compounds [1–3], among which up to ~20% (wt) can be aromatics [1]. The distillation curve of typical jet fuels gives hints about the presence of high molecular weight species in the fuel, some of which are polycyclic in nature [4–6]. For a typical Jet A, the temperature at the 90% distillation volume is around 250 °C [4], which exceeds the boiling point of naphthalene (218 °C) and tetralin (208 °C). The impact of multi-ring species on soot formation is apparent through a range of previous studies of soot formation, most of which were conducted in counterflow or coflow diffusion flames [7–18]. In many of these studies, gaseous-fueled baseline flames were doped with low concentrations of vaporized liquid jet fuels and their surrogates, demonstrating the effects of dopant chemical composition on sooting tendencies while preserving the main properties of the baseline flames (e.g. temperature, velocity) [11,13–16,18]. With the motivation to identify simple surrogates capable of reliably predicting the sooting behavior of kerosene, Moss and Aksit [7,12] conducted an experimental investigation on the sooting, laminar, and turbulent coflow flames of aviation kerosene and blends of *n*-decane with a range of alkyl-substituted aromatics. The sooting behavior of the surrogates was also compared on the basis of the measured smoke points. They found that a mixture of 30% (mass) mesitylene or propylbenzene and 70% (mass) *n*-decane represents the sooting behavior of an aviation kerosene well in both laminar and turbulent flames. Saffaripour et al. [8] studied coflow diffusion flames of pre-vaporized Jet A-1 and four synthetic jet fuels to compare their sooting characteristics and flame structures. They showed that soot levels along the centerline of coflow diffusion flames are strongly correlated to the aromatic content of the fuel, and soot and acetylene concentrations are not proportional to each other. In more recent studies, Saffaripour and coworkers [9,10] measured soot volume fraction in a Jet A-1 coflow diffusion flame and compared it with the

---

[*] Corresponding author.
E-mail address: haiwang@stanford.edu (H. Wang).

[1] Current address: Department of Mechanical and Process Engineering, ETH Zurich, Switzerland.

[2] Current address: Department of Mechanical Engineering, San Diego State University, San Diego, CA 92182, USA.

https://doi.org/10.1016/j.fuel.2018.07.099
Received 8 May 2018; Received in revised form 20 July 2018; Accepted 22 July 2018

volume fraction observed in a corresponding flame burning a surrogate that is comprised of 69% (mol) *n*-decane, 20% *n*-propylbenzene and 11% *n*-propylcyclohexane [19]. They found that such a surrogate underpredicts the soot concentrations of the real Jet A-1 up to a factor of five, and the same trend was observed in the smoke points of these fuels. Consequently, they suggested that the addition of two-ring aromatics is necessary in order for the surrogate to reproduce the sooting propensity of the real Jet A-1. In the work of Witkowski et al. [11], soot volume fraction and morphology measurements were made in a laminar coflow methane-air diffusion flame seeded with approximately 2200 ppm of a real Jet A and the first-generation MURI surrogate [20] in which the aromatic component is represented by 24% by volume of toluene. The surrogate jet fuel was shown to have notably lower soot volume fractions than the real Jet A. In the work of Lemaire et al. [21], soot volume fraction in turbulent diffusion flames burning kerosene and its surrogate was measured and compared. It was shown that a surrogate containing decalin, a two-ring compound, is required to reproduce the sooting behavior of real jet fuels.

The evolution of main oxidation products and soot precursors in methane and ethylene flames doped with small amounts of jet fuel and surrogate mixtures was extensively studied also in counterflow flames [14–16,18]. For example, Honnet et al. [17] measured soot volume fraction in laminar non-premixed flows burning a JP8 and the Aachen surrogate comprised of 80% *n*-decane and 20% 1,2,4-trimethylbenzene by mass. They found that the Aachen surrogate reproduces the sooting tendency of JP-8 well within the range of the flame conditions studied.

As discussed above, surrogate fuels have become a widely used approach for dealing with the challenges of modeling real fuels. Most of the studies on jet fuels aimed at formulating surrogate mixtures capable of reliably predicting chemical and physical properties of common aviation fuels, such as volatility, boiling point curves, smoke point, advanced distillation curves, average molecular weight, H/C ratio, the derived cetane number, and the threshold sooting index (TSI) [22]. Dooley et al. [23] utilized the TSI, along with the average fuel molecular weight, H/C ratio, and derived cetane number, as targets to match a 4-component surrogate to a target Jet A fuel (POSF 4658). The components of the surrogate were blended in proportions, which minimizes the difference in the aforementioned targets between the fuel and its surrogate. The performance of the surrogate was compared to the real fuel in several controlled combustion experiments, including a wick-fed laminar diffusion flame, which was used to measure the smoke points of the fuel and surrogate. Additionally, soot volume fractions in the flame were quantified using laser light extinction; the peak of volume fraction values was found to be comparable for the Jet A fuel and the surrogate at their respective smoke points.

The aromatic content of a fuel is an important practical indicator of its sooting tendency [24]. This has motivated attempts to match the proportion and distribution of aromatics between a real fuel and its surrogate as a way to ensure a wide range of applicability of the fuel surrogate. Importantly, it has been noted that the sooting tendency of real fuels correlates well with their aromatic content as long as the ratio of polyaromatics/monoaromatics is similar between the real fuel and the surrogate. In a recent work [25], sooting tendencies of several jet fuels and their surrogates were experimentally measured in terms of the Yield Sooting Indices (YSIs). It was found that while the sooting behavior of a fuel is largely dependent on the aromatics present in the fuel, a lumped parameter such as the aromatics volume percent can be inadequate for predicting the fuel sooting tendency. To develop surrogates with fidelity to mimic the sooting behavior of real fuels, it is important to characterize the nature of their aromatic content.

We wish to point out here a simple fact that has not received sufficient attention in earlier studies, namely the role of the real-fuel distillation curve in soot formation. As observed in the work of Bruno and coworkers [4], there is a continuous drop in the content of one-ring aromatics and a simultaneous increase in the content of the two-ring aromatic compounds towards the high boiling-point fractions. The very tail end of the distillation curve can reach a temperature as high as 350 °C, which is in the range of the boiling points of high-molecular weight, three to four-ring aromatics (e.g., 340 °C for phenanthrene and 378 °C for pyrene). Obviously, these multi-ring compounds within the fuel are trace species but they still could shortcut the growth process of polycyclic aromatic hydrocarbons (PAHs) and in this way, induce soot nucleation in engines especially in non-premixed spray combustion. Currently, the composition of the tail end of the distillation curve is not well known, as available distillation curve studies typically stop at 90% volume fraction. A range of questions thus arise:

1) What is the nature of the fuel compounds in the tail end of the distillation curve and what role do they play in soot formation?
2) Jet fuels are utilized in practical systems as a spray, and the distillation curve must impact, at least in some cases, the local concentrations of the different constituents of the multicomponent fuels. Hence, can the sequential evaporation of the fuel components, from low to high boiling points, produce transient, spatial enrichment of multi-ring fuel components, thus impacting soot nucleation and growth?

The current work aims to address a range of related questions surrounding the effect of the likely existence of multi-ring species on soot formation from real jet fuels. We carry out our studies across three laboratory flame platforms, from laminar premixed stretch-stabilized flames to the counterflow and coflow diffusion flames. One of our emphases was to examine the sooting properties of different distillate fractions of a typical Jet A. A comparison of the sooting properties of the Jet A and the 2nd generation MURI surrogate (40% *n*-dodecane, 29% *iso*-octane, 7% 1,3,5-trimethylbenzene and 23% *n*-propyl benzene by mole) [23] is also presented and discussed to shed light on the above questions.

2. Methodology

2.1. Distillation setup

The fuel investigated in this study is an average commercial Jet A, designated as POSF 10325 [1], which is basically POSF 4658 [4,6]. In order to understand the impact of the different distillation fractions on the sooting property, a range of the distillate fractions was obtained by distillation. The setup and procedure follow that of Bruno and coworkers [4–6] with small modifications to ensure reliable output in the volume fraction range of 90–100%. As depicted in Fig. 1, a round-bottom flask was filled initially with 400 ml of Jet A. The liquid was

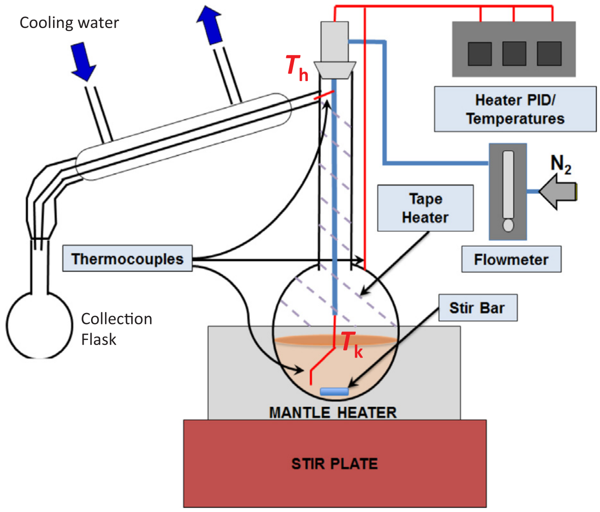

Fig. 1. Schematic diagram of the distillation setup.

stirred and heated from room temperature to 360 °C using a temperature controller. In earlier distillation experiments [26,27], both N_2 and Ar were used to prevent fuel oxidation, with Ar providing somewhat better results. In our measurements, a flowrate of 0.4 SCFH of N_2 was used for purging the flask from the onset of heating and maintaining an inert environment, even though Ar may be more effective than N_2. Vaporized fuel passes through the distillation head, condenses in a water-cooled glass Graham condenser, and is collected in a calibrated flask, in which the volume measurement is made. Thermocouples were used to measure the boiling flask (kettle) temperature (T_k, the liquid temperature) and the head temperature (T_h, the temperature of the vapor at the bottom of the takeoff position in the distillation head). The temperatures were recorded at each of the predetermined distillate volume fractions. The one-standard deviation in T_k fluctuation was approximately 0.6 °C, and that in T_h was approximately 3 °C. The actual uncertainty in T_h is larger than 3 °C, of course, due to the difficulty in placing the thermocouple in the exact same location in the distillation head. Other factors include turbulence, uniformity of vapor flow and radiative heating from the glass.

Jet A was distilled first into 8 distillate volume fractions (0–60%, 60–70%, 70–75%, 75–80%, 80–85%, 85–90%, 90–95% and 95–100%). The last fraction was distilled further, thus obtaining three separate distillate (95–97.5%, 97.5–98.75%, 98.75–100%). The density of each fraction was measured and the composition was analyzed using gas chromatography–mass spectrometry (GC–MS). The molecular weight (MW) and hydrogen-to-carbon (H/C) ratio were empirically estimated according to the dependence of MW and H/C ratio on density among several jet fuels (see Fig. S1 of the Supplementary Materials):

$$\mathrm{MW(g/mol)} = 450.97\rho^2 - 422.58\rho + 207.14$$

$$\mathrm{H/\ C} = 38.545\rho^2 - 64.494\rho + 28.845$$

where the density ρ is in g/cm^3. The above equations are valid for $0.78 \le \rho\ (g/cm^3) \le 0.827$.

2.2. Premixed stretch-stabilized flame

Setup of the premixed stretch-stabilized stagnation flame is based on the setup introduced in a previous work [28] with the difference being the addition of a fuel vaporization system. As shown in Fig. 2, the burner is comprised of an aerodynamically shaped nozzle, 1.43 cm in exit diameter, a stagnation surface/sampling probe assembly and a scanning mobility particle sizer (SMPS). The aerodynamic shape of the burner nozzle body was designed to achieve a plug flow at the burner exit. The distance between the burner nozzle and stagnation plate, L, was held constant at 1.0 cm. The standing distance between the flame and the stagnation surface/sampling probe, L_s, and hence the reaction time beyond soot nucleation is varied by changes in the unburned gas velocity.

Similar to the burner-stabilized stagnation flame sampling technique [29,30], the water-cooled stagnation surface also acts as a sampling probe. The temperature at the stagnation surface, T_s, is measured by a type-K thermocouple placed flush with the surface such that the bead is exposed to the sample gas at a radial distance of 1 cm from the centerline of the flame. The stagnation surface temperature is $T_s = 368 \pm 25$ K for all flames tested herein. The gas temperature at the nozzle exit T_n was also determined by a type-K thermocouple and is 513 ± 10 K for all flames studied. The uncertainty values quoted here are one standard deviation.

Soot mobility particle size distribution functions (PSDFs) were measured at the stagnation surface on the center axis of the flame. A micro-orifice (127 µm diameter, 125 µm wall thickness) embedded within the stagnation plate continuously draws a particle-laden gas flame sample, which is quickly diluted by a flow of cold nitrogen thus quenching the reaction and preventing particle losses by coagulation. An optimum dilution ratio (DR) was determined following the procedure of previous studies [28,29]. The ratio was held constant for each flame (DR ~ 10^3). Mobility PSDFs are determined by an SMPS (TSI 3080). Corrections for multiple charges and diffusion loss were made within the Aerosol Instrument Manager software. The size of particles smaller than 10 nm can be overestimated by the software due to the limitation of Cunningham slip correction [31]. The mobility diameter was corrected by the relationship as discussed in [32] on the basis of an improved transport theory [33,34]. In these stretch-stabilized premixed flames, nascent soot particles, as defined in [35], are probed.

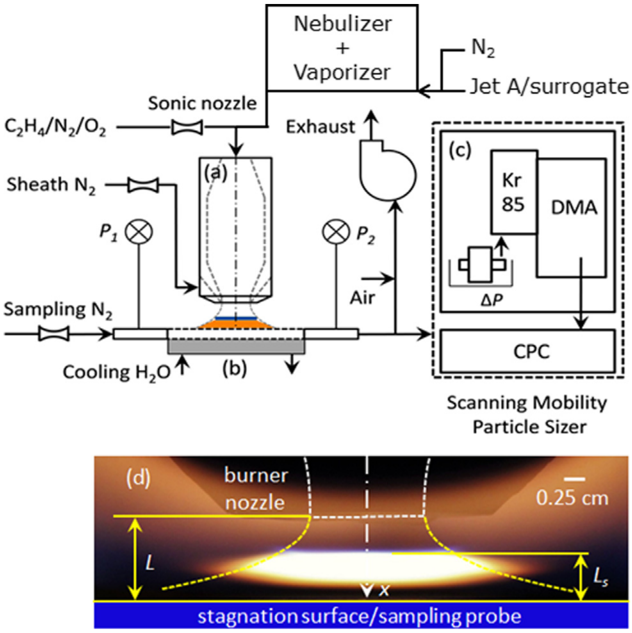

Fig. 2. Schematic showing various parts of the experimental setup. (a) Burner nozzle, (b) sampling probe/stagnation surface, (c) Scanning Mobility Particle Sizer (SMPS), (d) a typical image of Jet A doped flame (adapted from ref. [28]).

Three series of host flames (*a*, *b* and *c* as shown in Table 1) were examined for each jet fuel tested, varying the unburned gas velocity while keeping all other flame parameters constant. The variation in the unburned gas velocity has the effect of changing the flame standoff distance, and thus it impacts the particle residence time in the flame [28]. The host flames are all near-sooting ethylene-oxygen-nitrogen flames (12.2% C_2H_4, 17.8% O_2, and 70% N_2, $\phi = 2.06$) in which a given liquid fuel is doped into the unburned mixture at two levels of dopant concentrations (series *i* and *ii*). The liquid fuels tested are Jet A as received, its light distillate fraction from 0 to 60% and the residue distillate fraction from 95 to 100%, and the 2nd generation MURI surrogate [23]. A limited number of experiments were carried out also for the 98.75–100% distillate fraction. Because the H/C ratios of the liquid fuel tested, including the 98.75–100% distillate fraction, are not significantly different from each other, as will be discussed later, the equivalence ratio of the unburned mixture stays the same at a given mass doping of the liquid fuel. These are $\phi = 2.18$ at 7260 ppm and $\phi = 2.24$ at 11500 ppm mass doping. The various flame parameters and the jet fuel dopants studied are summarized in Table 1. The flames are labeled by "host flame series"-"liquid fuel"-"dopant mass fraction series." For example, *a*-Jet A-*i* refers to a doped flame that has a cold gas velocity of 50.3 cm/s (see Table 1), with Jet A as received as a dopant at a concentration of 7260 ppm by mass; *c*-(95–100%)-*ii* refers to a doped flame that has a cold gas velocity of 39.7 cm/s, with the 95–100% distillate fraction as a dopant at a concentration of around 11500 ppm by mass.

Liquid fuel was metered using a syringe pump (Harvard PHD2000), vaporized at 483 K, and mixed with the remaining gas components, as

Table 1
Flame parameters of the stretch-stabilized premixed flames, and physical properties of the jet fuels or surrogate used as the dopants (ρ: liquid mass density, MW: mean molecular weight).

Cold gas velocity,[a] v_o (cm/s)			**Host-flame unburned gas**, mole %		
series *a*	series *b*	series *c*	C_2H_4	O_2	N_2
50.3	45.2	39.7	12.2%	17.8%	70.0%
Dopant	ρ (g/cm^3)	**MW** (g/mol)	**Dopant mass fraction** (ppm)[b]		
			i (ϕ = 2.18)	*ii* (ϕ = 2.24)	
Jet A					
as received	0.803	158.6	7260 ± 5	11490 ± 15	
0–60% fraction	0.786	153.5	7260 ± 9	11490 ± 9	
95–100% fraction	0.818	163.1	7260 ± 7	11490 ± 11	
98.75–100% fraction	0.824	165.1	–	11500 ± 9	
2nd gen surrogate[c]	0.758	138.7	7260 ± 15	11510 ± 45	

[a] STP condition (298 K, 1 atm). The cold gas velocity includes the contribution from the liquid dopant. The temperature of the unburned gas is maintained at 513 ± 10 K, and that of the stagnation surface is 368 ± 25 K.

[b] Mass doping in the unburned mixture. The overall equivalence ratios are ϕ = 2.18 (series *i*) and ϕ = 2.24 (series *ii*).

[c] The surrogate is composed of 40% *n*-dodecane, 29% *iso*-octane, 7% 1,3,5-trimethylbenzene and 23% *n*-propyl benzene by mole [23].

described in Ref. [36]. All unburned gas lines were maintained at 483 K and the burner temperature was set at 513 K. The nitrogen sheath flow velocity matches the cold, unburned gas velocity for each flame to minimize flame edge effects [28].

The premixed stretch-stabilized flame is pseudo-one dimensional and amenable to numerical simulation [28]. We used OpenSMOKE++ [37] for this purpose, with the boundary conditions appropriate for the underlying problem. The HyChem Jet A reaction model [2,38] was used to describe the reaction kinetics of Jet A.

2.3. Non-premixed counterflow flame

A counterflow burner facility was employed to study soot formation in non-premixed flames [39–41]. This facility consists of two aerodynamically converging opposing nozzles 1.0 cm in exit diameter. The nozzle to nozzle separation distance is 1.1 cm. The fuel and oxidizer streams were both diluted with nitrogen. Liquid jet fuel or one of its distillates was injected using a liquid pump with 0.5% accuracy and vaporized in an annular coflow of nitrogen at 503 K in a vaporization chamber. Both the fuel and oxidizer streams were maintained at T_u = 400 K to prevent fuel condensation.

Soot volume fraction (f_v) was measured by laser induced incandescence (LII) calibrated with light extinction measurement [39–41]. The light extinction measurements used a He-Ne laser and a refractive index value of $m = 1.57 - 0.56i$, a value widely adopted in the literature and also validated for various flames burning different fuels [39]. The corresponding $E(m)$ value is 0.26. In the LII measurement, an Nd:YAG laser (Continuum Powerlite 8010) with 10 Hz repetition rate provides a 532-nm laser beam, from which a laser sheet was formed by expanding it with a cylindrical plano-concave lens of 2.57 cm in focal length and a plano-convex lens of 25.0 cm. The energy distribution in the laser sheet is uniform due to the large vertical expansion; and the laser fluence is 0.58 J/cm^2. An iris was also used to let the central part of the laser sheet pass through the flame. The LII signal was detected at 450 nm by a Peltier cooled intensified CCD camera (Princeton Instrument, PIMAX-3). The detection wavelength was selected to avoid/minimize the interference from the C_2 Swan band emissions [42]. A delay of 25 ns was applied to the intensifier, corresponding to a 5 ns delay from the peak LII signal, to mitigate the interference of PAH fluorescence, while a gate width of 80 ns was selected to avoid the particle size bias in the LII signal. The standard deviation in the LII measurement was less than 18% based on 60 LII images.

Table 2
Parameters of the counterflow diffusion flames.[a]

Host flame composition: $X_F = X_{O_2}$		
0.40	0.35	0.30
Jet A dopant	**Dopant concentration** (ppm)[b]	
	mole	mass
as received	2000	11330
0–60% fraction	2000	10960
95–100% fraction	2000	11650

[a] Nitrogen as the balance gases in both fuel and oxidizer jets at 400 K. All flames are at a global strain rate of 200 s^{-1}.

[b] Concentration in the fuel stream.

The test conditions are shown in Table 2. The host counterflow diffusion flames were established with a fuel stream of C_2H_4/N_2 flowing against an oxidizer stream of O_2/N_2. The global strain rate was maintained at $K = 200\ s^{-1}$, thus keeping the characteristic residence times experienced by the reactants in the combustion zone the same across all test conditions. The mole fraction of C_2H_4 in the fuel stream, X_F, and the mole fraction of O_2 in the oxidizer stream, X_{O_2}, were kept equal. There are three series of flames (*a*, *b* and *c* as shown in Table 2): two sooting conditions, $X_F = X_{O_2} = 0.40$ and $X_F = X_{O_2} = 0.35$, and one near-sooting condition of $X_F = X_{O_2} = 0.30$, which were selected for the host flames. Jet A or a certain distillate fraction was doped into the fuel stream at the concentration of 2000 ppm by mole. In the doped flames, the ethylene mole fraction was slightly reduced and accordingly to keep the total fuel mole fraction and thus the total fuel jet velocity the same between the doped and host flames. The mass fractions of the doped jet fuel differ somewhat because of the difference in the fuel molecular weight. The stoichiometric mixture fraction (Z_{st}) values of the three host flames and the doped flames are all around 0.24, indicating the similar flame location for all tested conditions.

2.4. Non-premixed coflow flame

A co-annular burner assembly was used to produce atmospheric pressure laminar co-flow diffusion flames [43]. Briefly, the burner consists of an inner tube 1.09 cm in inner diameter (ID), 0.09 cm in wall thickness, and a concentric 9 cm ID annulus for the oxidizer flow. We use ethylene diluted in nitrogen to establish the host flame and air as the oxidizer flow. Jet fuel or its distillate is added to the ethylene-nitrogen jet in doped flames. A syringe pump (Harvard PHD Ultra) was used for liquid fuel delivery. The liquid fuel was vaporized by the Bronkhorst CEM Liquid Delivery System into a nitrogen stream, which is then mixed with ethylene downstream of the vaporizer. The fuel mixture was conveyed by a heated tube at 541 K to prevent condensation. The flame conditions are presented in Table 3. Images of the flames are presented in Fig. S3 of the Supplementary Materials.

Spectral Soot Emission (SSE) measurements [44] were made to obtain the flame temperature, as described in Ref. [43]. A Princeton Instrument SP2105i spectrometer accompanied by PIXIS100 digital camera was used to capture the local spectral radiance collected by an optical assembly consisting of an achromatic lens with a fixed focal length of 10.0 cm and an iris with an aperture of 0.2 cm. The temperature was then obtained from recovering local property fields using the Abel Inversion via the Nestor-Olsen Algorithm [45]. The absorption coefficient, $E(m)$, was assumed to be a constant and equal to 0.26 [44]

Table 3
Non-premixed coflow flame conditions.

	Host flame	Doped flames[a]
Inner fuel flow		
C_2H_4, L/min[b] (g/h)	0.19 (13.0)	0.17 (11.4)
Liquid fuel, g/h		1.7
Diluent N_2, L/min[b]	0.5	0.5
Outer oxidizer flow (L/min)[b]	60	60

[a] The dopants are jet A as received, its 0–60% and 95–100% distillation fractions.

[b] STP condition of 298 K and 1 atm. The unburned fuel-nitrogen jet is maintained at 541 K.

for the wavelength range of 491.8–994.8 nm used in the SSE measurements.

A modified Artium LII-200 time-resolved LII system, as described in [43], was used to obtain local soot volume fraction (f_v) and soot primary particle diameter (D_p). The system has an Nd-YAG laser centered at the wavelength of 1064 nm. Soot volume fraction measurements are made at a fluence of 0.1 J/cm^2. The LII system has default values of 0.4 for $E(m)$ and 0.26 for the thermal accommodation coefficient, α_T. The latter is needed for interpreting the LII measurements in terms of particle diameter. Soot volume fraction (f_v) can be computed from the peak soot temperature and D_p can be estimated from the temporal decay of the soot temperature to the flame temperature, which was obtained separately by the SSE as described earlier. The method to determine particle diameter is only sensitive to mature soot particles with solid appearance with primary particle diameter as small as 10 nm.

The SSE temperature measurements are subject to two sources of errors: emission attenuation and background radiation. The basic theory of SSE assumes that emission attenuation can be neglected [44]. However, this can be an issue in the core region of flames with strong annular soot profiles, whereas the impact of emission attenuation is insignificant in the annulus regions. Background radiation is more likely to be significant at locations where the local emission-to-peak local emission is small [46]. Thus it is believed that, for soot profiles that are strongly annular, the core region and the outer edge of the annulus are more sensitive to background radiation. In the current study, since the local emission in the core region is still strong, the background radiation is insignificant. However, in the outer region of the annulus ($r > r_{T\max}$), the measurements are strongly influenced by background radiation and therefore are ignored. The SSE technique may also suffer from the errors induced by the inversion algorithm. For annular soot profiles, the Abel Inversion causes noises in the temperature profile in the core region. In these cases, the measurements in the core region are therefore ignored. In general, in the regions where sufficient soot is present, the temperature measurements by the SSE technique agree well with other measurement techniques such as coherent anti-Stokes Raman scattering (CARS) and rapid thermocouple insertion (RTI) [44,46].

It is known that $E(m)$ is subject to some uncertainty. In these measurements, the $E(m)$ values are chosen to be 0.4 for LII and 0.26 for SSE. The difference is due to variations in soot maturity, with mature soot having higher $E(m)$ values. LII heats and anneals soot [43,50], causing soot graphitization [43,50] and thus a higher $E(m)$ value. The value chosen is close to the upper end of the $E(m)$ range (0.15–0.41) known for soot particles [47–49].

The reproducibility of the data was investigated. Single-shot variation was greatly reduced by averaging approximately 500 single-shot measurements at each location. The measurements at each location will also vary day to day because of small errors in the positioning and flow systems. This repeatability was evaluated by calculating the 95% confidence interval for the distance from the mean using a paired t test. Thus, the repeatability was calculated to be within ± 0.03 ppm for the soot volume fraction based on 102 pairs of different day measurements. The repeatability was calculated to be within ± 0.27 nm for the soot primary particle diameters (D_p) based on 44 pairs of different day measurements. These repeatability intervals are shown as the error bars on the figures. Another possible source of error in the D_p value could be caused by the fact that its estimation relies heavily on particle specific surface area available for conduction, which does not account for size distribution and particle aggregation [51]. The shielding and bridging effects, which refer to the hidden primary particles inside soot aggregates and bridges among primary particles, may also contribute to the error [43,51]. The absolute errors are mainly attributed to the choice of $E(m)$. It is possible that there are variations in the optical properties of the soot with flame location and different fuels; a quantitative knowledge of this variation is currently unknown. However, as fuels were compared under the equal settings, we believe that this uncertainty will not significantly affect our conclusion.

During the experiment, f_v along the centerline of each flame was measured and the height that produces the maximum centerline f_v, denoted as HAB$_{fv,\max}$, was identified for each flame. The HAB$_{fv,\max}$ values are 4.8 cm for the host flame, and 5.5 cm, 5.6 cm, and 5.4 cm for flames doped with Jet A as received, its 0–60% distillate fraction and 95–100% distillate fraction, respectively. Selected radial temperature profiles can be found in Fig. S4 of the Supplementary Materials.

3. Results

We focus the discussion on the stretch-stabilized premixed flames first with two related components: evaluating the accuracy of the 2nd generation MURI surrogate in reproducing the detailed sooting properties of the Jet A tested and examining the variation of the sooting tendency with respect to Jet A distillation fractions. To shed light on the second component of the study, the dependency of sooting tendency on Jet A distillation fractions is further studied in laminar diffusion flames in the counterflow and coflow configurations.

3.1. Stretch-stabilized premixed flame structures

Axial velocity and temperature profiles computed for the host ethylene flames doped with Jet A are shown in the top panel of Fig. 3. The maximum temperatures are all around 1900 K in host flames *a*, *b* and *c*. The preheat zone of the flame is not attached to the burner, which is typical for stretch-stabilized flames. Rather, the rise in temperature occurs where the local flow velocity approaches the laminar flame speed of the underlying unburned mixture. The variation in the unburned gas velocity corresponds to changes in the global strain rate of the flame, which in turn causes the flame standing distance and the particle residence time to vary within each series of the flame [28]. The flame structure is similar across the range of the cold gas velocity used. As an example, numerical solution of selected major and minor species of Flame *c*-Jet A-*i* is shown in the bottom panel Fig. 3.

3.2. Jet A versus the 2nd generation MURI surrogate in premixed stretch-stabilized flames

In general, the particle size distribution functions measured for the stretch-stabilized flames can be described well by a bi-lognormal distribution [28] even though all of the PSDFs observed here are unimodal. In the form of volume distribution (nm^3/cm^3), we have

$$\frac{dV}{d\log D_m} = \sum_{i=1}^{2} \frac{V_i}{\sqrt{2\pi}\,\log\sigma_{g,i}} \exp\left[-\frac{(\log D_m - \log\langle D_m\rangle_i)^2}{2(\log\sigma_{g,i})^2}\right],$$

where V is the volume fraction of the particles in the mobility diameter D_m range of $\log D_m$ to $\log D_m + d\log D_m$, V_i, $\sigma_{g,i}$ and $\langle D_m\rangle_i$ are the volume fraction, geometric standard deviation and median mobility diameter of the i^{th} particle mode, respectively. In obtaining the volume distribution, we assume that all particles are spherical such that $dV = dN(\pi D_m^3/6)$.

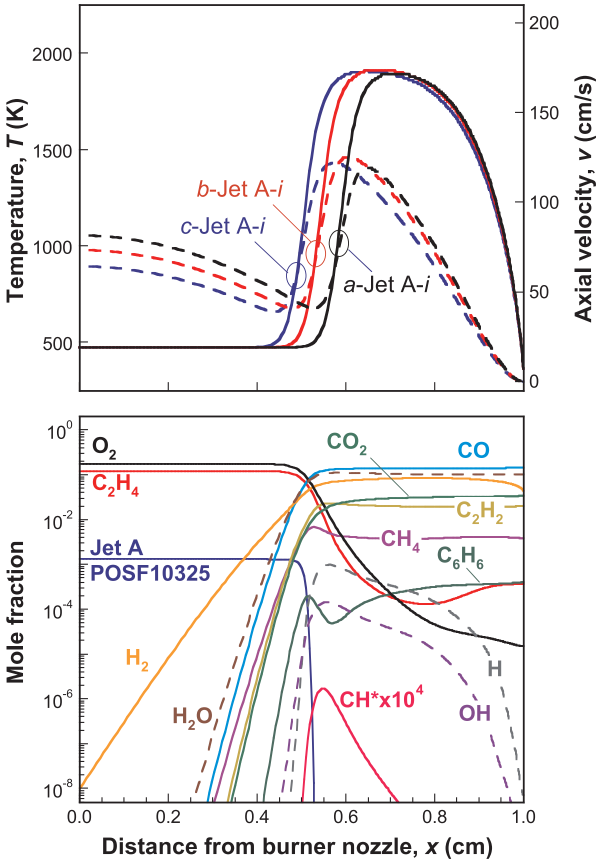

Fig. 3. Top panel: profiles of temperature (solid lines) and velocity (dashed lines) computed for the premixed stretch-stabilized flames (the Jet A-*i* series); bottom panel: profiles of species mole fraction for the *c*-Jet A-*i* flame (see Table 1 for the flame conditions).

Since the diameter D_m is the mobility diameter, the resulting volume fraction is called the mobility volume fraction hereafter. Quantitatively, this volume fraction is not identical to that measured by LII (to be discussed later). As discussed in recent works [29,52,53] soot particles are found to deviate from sphericity even at the early stage of growth. Hence the spherical assumption gives an upper estimate of soot volume fraction and comparisons of soot volume fraction should be considered as being semi-quantitative. Fig. 4 shows the volume distribution functions measured for the ethylene flames doped with Jet A as received (the left panel) and the 2nd generation MURI surrogate (the right panel), both at 7260 ppm level of dopant concentration. A similar plot is presented in Fig. S2 of the Supplementary Materials for PSDFs observed at the higher level of doping (11500 ppm). In all cases, the median diameter of the second size mode $\langle D_m \rangle_2$ increases with a decrease in the cold gas velocity from flame series *a* to *c* for a given fuel, as expected due to an increased reaction time.

The soot produced from the surrogate is notably lower than from Jet A under comparable conditions, both in the number density and median diameter of the particles. For comparison, in the *c* series of flames (39.7 cm/s cold gas velocity) the median diameter of the second size mode is 5.93 nm with Jet A doping and 3.79 nm with the surrogate. Fig. 5 presents the comparisons of the soot volume fraction (f_v) obtained by integrating the respective PSDFs of Fig. 4. It is seen that Jet A produces two to three times more nascent soot than the MURI surrogate at the high gas velocities (series *a* and *b*), and a four-fold increase of nascent soot at the lower end of the gas velocity tested (series *c*). The levels of discrepancy in f_v between Jet A and the MURI surrogate are similar at the higher doping of 11500 ppm. Moreover, the influence of cold gas velocity on the soot volume fraction of the surrogate flame is less evident than that of Jet A flame. Since the partiles probed here are just beyond nucleation, the surrogate containing just the 1-ring aromatics does not reproduce the stronger nucleation observed from the Jet fuel, which contains multi-ring aromatics. The evidence presented here is a clear indication that matching the TSI of a jet fuel, among its other properties, does not guarantee the surrogate fuel to reproduce the real-fuel sooting tendency. Since the PSDFs observed here are all for nascent soot, the difference is attributable to the greater nucleation tendency of the jet fuel than its surrogate.

3.3. Distillation curve and distillate fraction properties

To isolate and explore the effect of heavier aromatic compounds on soot formation and growth, Jet A was distilled into several distillate volume fractions. Soot measurements were then made for selected fractions. Properties of Jet A and its distillates from the lightest fraction (0–60%) to the heaviest fractions (95–100% and 98.75–100%) and the average kettle temperatures for each distillate fraction are reported in Table 4. The variations of the mass density as a function of T_k and the distillation curve are presented in Fig. 6. The distillation curve reported by Lovestead Ref. [4] is also included in the figure, showing that the current distillation procedure reproduces the earlier study completely. The current distillation curve extends into the heavy molecular weight range, from 90 to 100%. As seen in Fig. 6, T_k rises sharply in the last 10% of the distillate fraction, reaching 360 °C for the 98.75–100% fraction. Although the temperature of this heaviest fraction falls between the boiling points of phenanthrene and pyrene, the fact that the estimated H/C ratio remains close to 1.9 suggests that the compounds in that fraction remain to be mostly saturated hydrocarbon species, and that polycyclic aromatics of three rings and larger are absent.

The above results are consistent with the GC–MS measurements made on the distillate fractions (see Section S2 of the Supplementary Materials). They show that in the highest-boiling point fractions, the compounds relevant to enhanced soot nucleation are probably alkylated naphthalenes, and to a minor extent, alkylated biphenyls and fluorenes. As shown in Fig. 7, the fraction of alkyl benzenes decreases across the entire distillation curve; and the increase of *n*-paraffin and *iso*-paraffin contents is less significant than the increases in indanes, tetralins, and naphthalenes. The largest aromatic compounds were naphthalenes with up to four methyl sidechains. Within the 90–100% fraction the amount of naphthalenes with two and three additional carbons (e.g. dimethyl- and trimethyl-naphthalenes) increases while non-substituted naphthalene and methylnaphthalenes decreases. Hence, the highest-boiling point fractions are two-ring compounds but polycyclic aromatic hydrocarbons of three rings and larger are absent.

3.4. Variation of soot formation from different distillate fractions in stretch-stabilized flames

The PSDFs observed for the various distillate fractions are compared to those of the parent Jet A in Fig. 8. The particles measured are all nascent soot having median mobility diameter smaller than 15 nm. It is seen that the different distillate fractions do soot differently. Under all equal conditions, the heavier fraction causes stronger nucleation and produces larger particles than the light fraction in all flame series tested. Also included in Fig. 8 are the PSDFs observed for the MURI surrogate at the lower level of fuel doping. Clearly, the soot produced from the surrogate is lower even than the 0–60% distillate fraction of the Jet A.

The corresponding volume fraction data are presented in Fig. 9. As expected, the volume fraction in flames doped with Jet A (as received) lies between those from the 0–60% and 95–100% distillate fractions. As discussed before, the flames tested at a given level of fuel doping have nearly the same equivalence and H/C ratio. The difference observed in the soot volume fraction can only be the result of differences in the molecular components of the fuels. Keep in mind that in these premixed

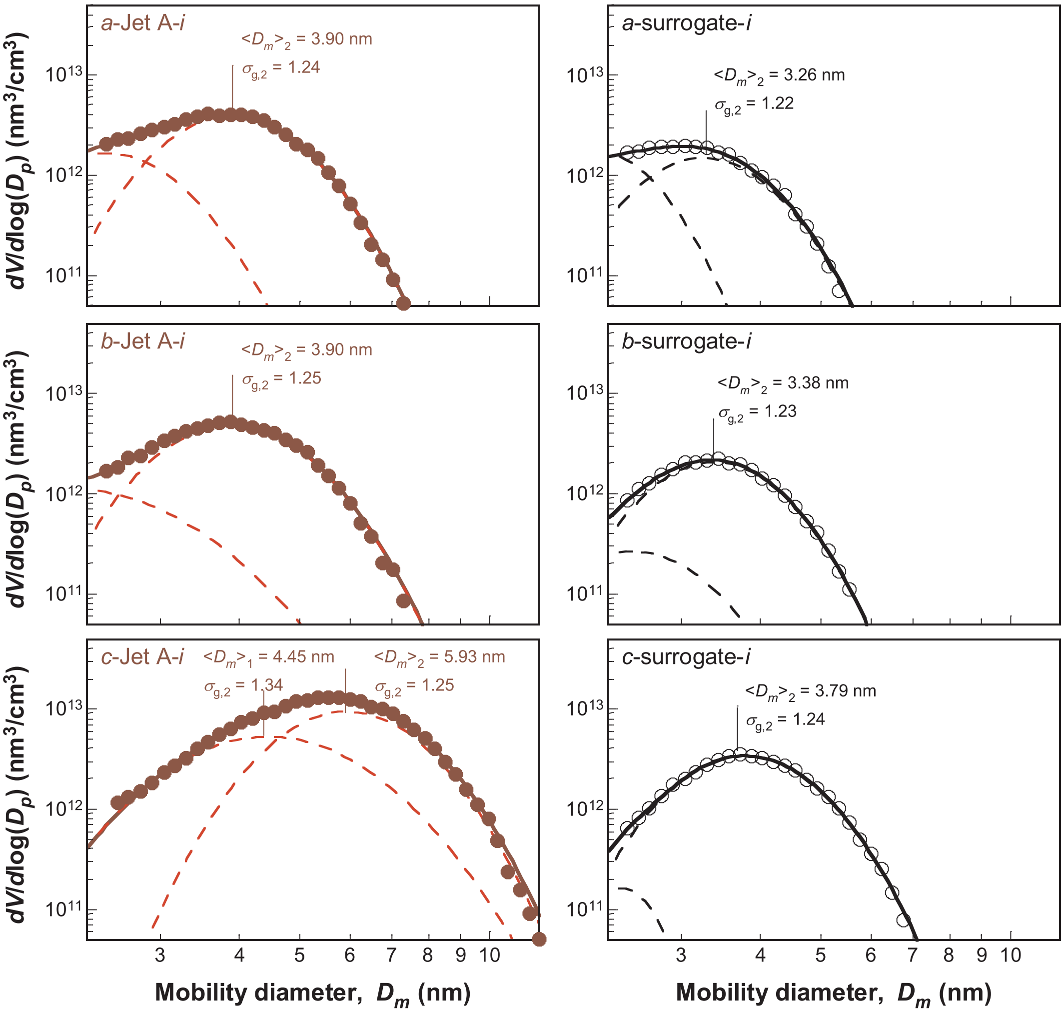

Fig. 4. Comparison of mobility volume distributions of nascent soot in three series of flames, comparing the sooting properties of Jet A as received with those of the 2nd generation MURI surrogate [23]. Symbols are experimental data averaged over three runs for each case; solid lines are bi-lognormal fits to the data; dashed lines are the respective first and second terms of the lognormal function.

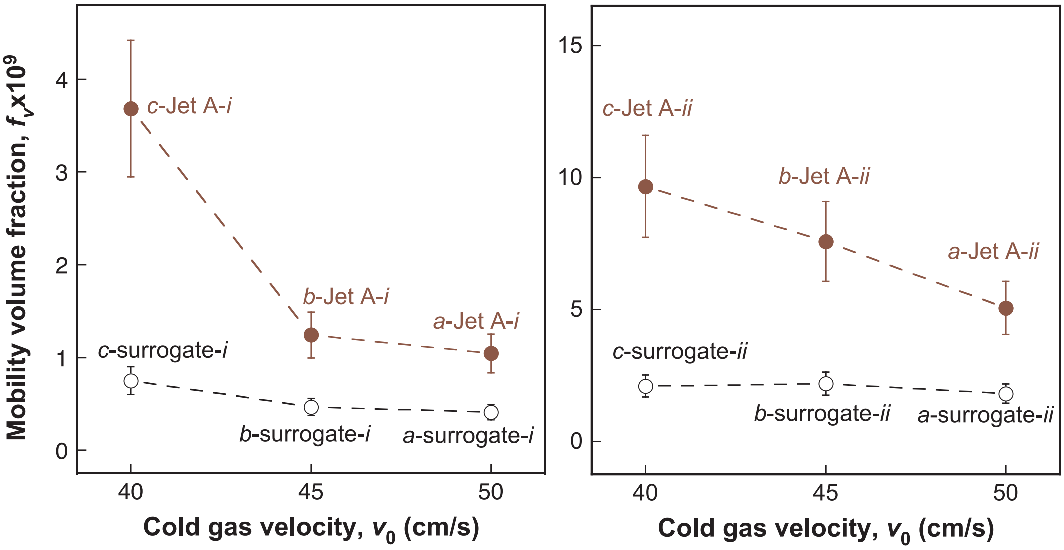

Fig. 5. Comparison of mobility volume fraction of nascent soot formed in the stretch-stabilized flame doped with Jet A (as received) and 2nd generation MURI surrogate. Left panel: 7260 ppm (mass) liquid fuel doping; right panel: 11500 ppm (mass) liquid fuel doping. Symbols are experimental data; lines are drawn to guide the eyes. The PSDFs at 11500 ppm (mass) liquid fuel doping is shown in Fig. S2 of the Supplementary Materials.

Table 4
Properties of Jet A (POSF 10325) and its distillate fractions.

Distillate vol. fraction (%)	Density[a] (g/cm^3)	MW[b] (g/mol)	H/C ratio[b]	T_k (°C)[c]
As received	0.803	158.6	1.91	–
0–60	0.786	153.5	1.97	223.3
60–70	0.797	156.7	1.93	231.8
70–75	0.800	157.6	1.92	236.1
75–80	0.801	157.9	1.92	241.8
80–85	0.802	158.3	1.91	248.8
85–90	0.803	158.6	1.91	255.5
90–95	0.807	159.8	1.90	267.6
95–100	0.818	163.1	1.88	
95–97.5	0.816	162.7	1.88	310.1
97.5–98.75	0.823	164.9	1.87	341.9
98.75–100	0.824	165.1	1.87	360.0

[a] The density of Jet A calculated from the density values measured for the distillate fractions is 0.793 g/cm^3, which is 1.26% lower than that of the Jet A as received.

[b] The mean molecular weight and H/C ratio are empirically estimated (see Section 2.1)

[c] 1-standard deviation is 0.6 °C.

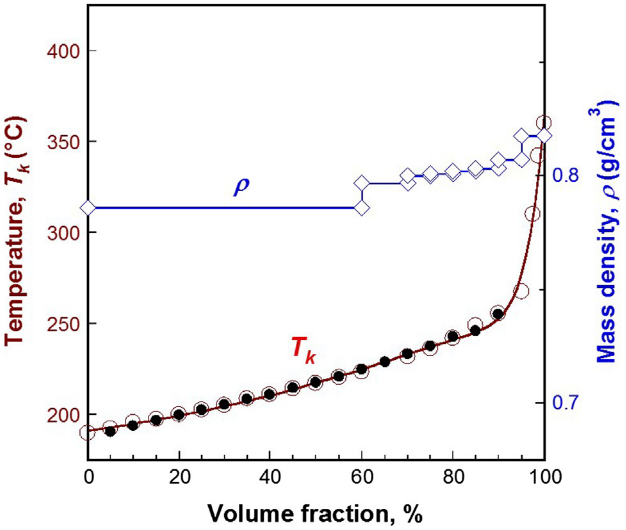

Fig. 6. Distillation curve (open symbols: this work, filled symbols: Lovestead et al. [4]) and mass density measured for Jet A (POSF10325). Symbols are experimental data; lines are drawn to guide the eyes.

stretch-stabilized flames, soot nucleates behind the flame with respect to the unburned mixture flow. Fuel components must pass through the flame layer before nucleation can occur; most of the heavy components must have been oxidized or undergo significant decomposition in the premixed flame. Even so, the difference in soot production is significant. It illustrates the role of the heavy or high-boiling point components in promoting soot nucleation. In particular, the fact that the 2nd generation MURI surrogate does not reproduce soot nucleation and early soot growth rate may be explained by the lack of two-ring compounds in its formulation – an issue already suggested in some of the earlier studies (see, e.g. [24,25]).

3.5. Counterflow diffusion flames

The top panel of Fig. 10 presents the spatially-resolved soot volume fraction profiles along the centerline of three undoped, baseline counterflow diffusion ethylene flames. It is seen that the overall soot layer thickness is similar and the soot volume fractions all peak around 0.34 cm from the fuel nozzle. Fig. 10 shows that both the total soot yield and the maximum soot volume fraction along the centerline, $f_{v,\max}$, increases with increasing X_F and X_{O_2}. Jet A or its distillate fractions was doped after a baseline ethylene flame was established. In order to ensure that the doped flame reached steady state, the LII signal was monitored from the moment of liquid fuel injection [54]. The signal increases sharply within the first two minutes and reaches a constant value after 14 min. The LII data were taken at 20 min after the moment of liquid fuel injection.

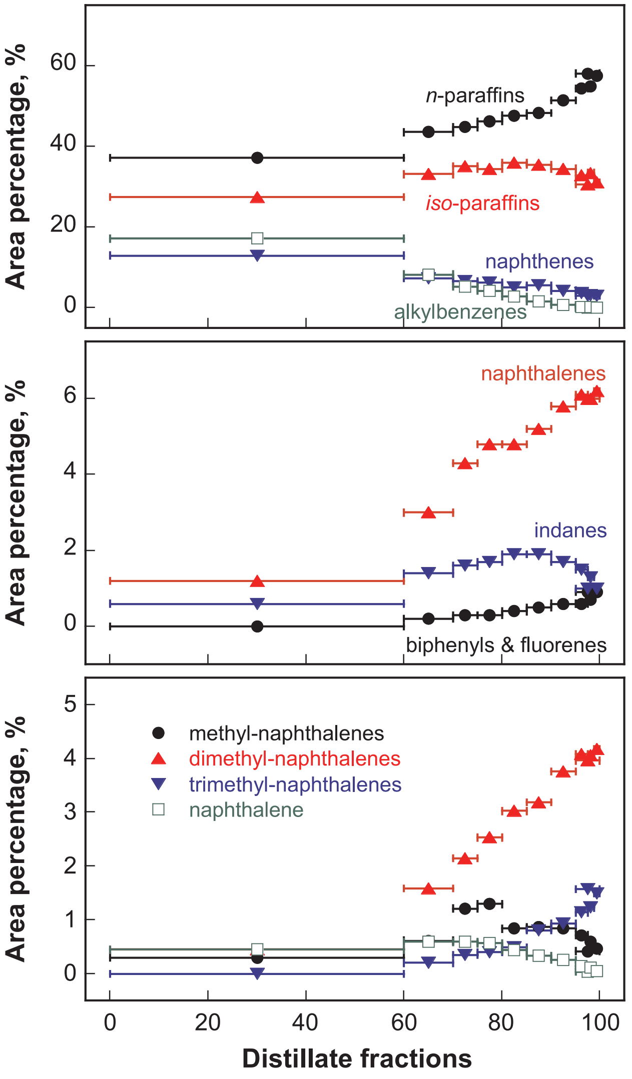

Fig. 7. Area percentages as determined from GC–MS characterization of the various distillate fractions of the Jet A fuel.

In the bottom panel of Fig. 10, soot volume fraction profiles are shown for the baseline flame at $X_F = X_{O_2} = 0.40$ and the corresponding doped flames. It can be seen that the profile thicknesses are again similar to each other among the flames studied, indicating that the level of dopant does not affect the flame structure significantly. When doped with Jet A, the peak soot volume fraction increases by about 30% from the undoped flame. The volume fraction profile in the flame doped with the 0–60% distillate fraction is almost the same as that of Jet A, suggesting that the nucleation and growth of soot are driven as much by the lower-boiling point components as the higher-boiling point components for the counterflow flame tested. For the same reason, the effect of the high-boiling point fraction on soot production is relatively mild. Doping with the 95–100% fraction causes the peak volume fraction to increase merely 30% compared to doping with Jet A as received.

Fig. 11 plots the variation of $f_{v,\max}$ as function of the volume percentage of the various distillate fractions in three baseline flames tested. Doping of Jet A or its distillates at 2000 ppm (mol) level generally leads

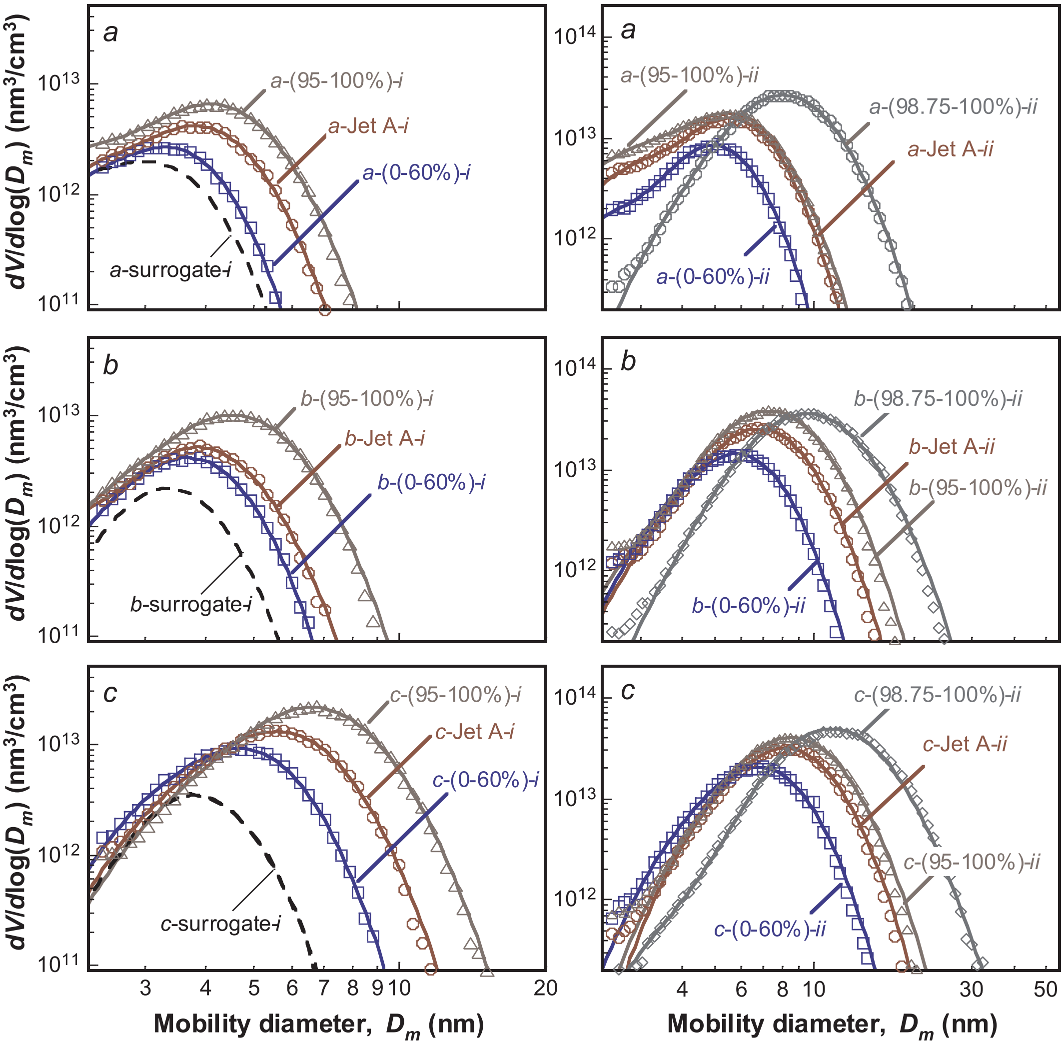

Fig. 8. Comparison of mobility volume distributions of nascent soot in series *a*, *b* and *c* flames doped with 7200 ppm by mass (left panel) and 11500 ppm by mass (right panel) of Jet A as received, and its 0–60%, 95–100% and 98.75–100% distillate fractions. Symbols are experimental data averaged over three runs for each case; lines are bi-lognormal fits to the data. The dashed lines in the left panel are mobility distributions of the 2nd generation MURI surrogate for comparable conditions.

to an increase in $f_{v,\max}$, but the impact of the high-boiling point components on soot production is gradual and mild. For the baseline flame at the lowest ethylene and oxygen concentration, i.e., $X_F = X_{O_2} = 0.30$, the variation of the maximum soot volume fraction is small and probably within the experimental uncertainty of the data across the distillation fractions tested.

3.6. Coflow diffusion flames

In Section 3.2, we used a series of premixed, stretch-stabilized flames to show that TSI is an ambiguous indicator of the sooting property of a jet fuel. In other words, matching the TSI and H/C ratio of a jet fuel does not guarantee that the surrogate fuel will reproduce the real-fuel sooting tendency. To shed light on this issue, we report here the results obtained in coflow diffusion flames with the expectation that the 2nd generation MURI surrogate reproduces the sooting properties of the jet fuel tested since TSI is measured in diffusion flames and therefore involves the same stages of soot production present in coflow diffusion flames. Indeed, Fig. S1 of the paper of Zhang et al. [55] shows that the soot volume fraction profiles of the 2nd generation MURI surrogate is very close to those of Jet-A POSF 4658. Moreover, as discussed in Hura and Glassman [56], the smoke point is determined by the competing processes of soot nucleation and growth and soot oxidation. Therefore TSI should be used with some caution as it measures the competing effects of two spatially separate processes. For this reason, probing the internal structure of the soot profile in a coflow flame is necessary to understand the sooting propensity of a fuel.

Images of the four coflow flames tested are shown in Fig. S3 of the Supplementary Materials. Parameters of the flames are listed in Table 3. All doped flames exhibit similar heights and the baseline flame is about 0.5 cm shorter. The onset of the yellow luminosity of the baseline, undoped flame was observed to be at higher HABs than those of the doped flames. Since the mass flow rates of the fuel(s) are nearly equal among the doped and undoped flames (see, Table 3), the HAB difference at the onset of luminosity indicates that the jet fuel and its distillates do generate more soot than ethylene.

Centerline soot volume fraction (f_v) profiles shown in the left panel of Fig. 12 provide a quantitative comparison of the relative sooting tendency of the four flames. The doped flames (Jet A as is, and the 0–60% and 95–100% distillate fractions) have significantly higher soot volume fraction compared to the base flame, highlighting the importance of fuel structure and composition on soot formation. The significant difference between the doped and baseline flames can be explained by an earlier soot nucleation and higher particle growth rates as a result of the presence of aromatics in the fuel. Soot nucleation occurs at lower heights in flames when aromatic compounds already

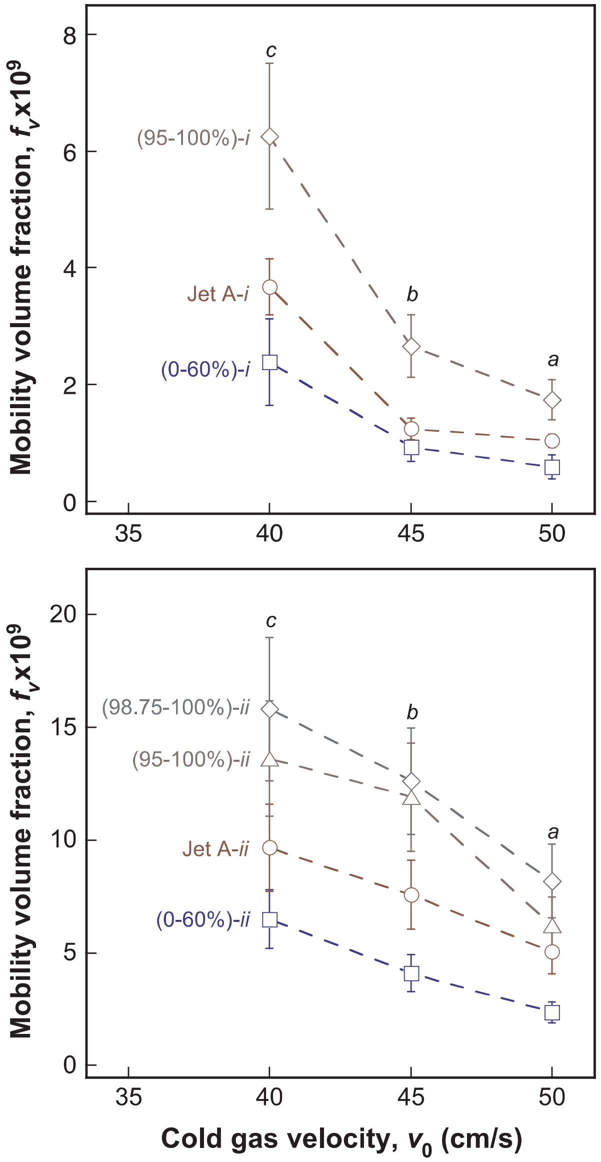

Fig. 9. Mobility volume fraction of nascent soot measured at the stagnation surface in host flames doped with 7200 ppm (mass) (top panel) and 11500 ppm (bottom panel) of Jet A as received (0–100%), and its 0–60% and 95–100% distillate fractions. The bottom panel also includes the data taken for the 98.75–100% distillate fraction of Jet A. Symbols are experimental data; lines are drawn to guide the eyes.

exist in the fuel stream. Similar phenomenon was observed by Zhang et al. [57,58], who studied the addition of *n*-propylbenzene into *n*-dodecane laminar coflow diffusion flame.

Soot concentration profiles of the jet fuel as received are not significantly different from its distillate fractions. The volume fraction from the flame doped with the 95–100% distillate fraction is moderately higher than that of the jet fuel as received, which in turn, is higher than that from the 0–60% fraction. It is likely that this reduced sensitivity toward the distillate fraction is caused by the relatively longer periods of particle growth (more than 100 ms for the flame tested) over particle nucleation than in premixed flames. The dominance of surface growth (as opposed to coagulation) is consistent with the observation that the primary particle diameters are all nearly equal among the three flames studied, as illustrated in the right panel of Fig. 12 for measurements on the centerline as well as in the wings as shown in Fig. S5 of the Supplementary Materials.

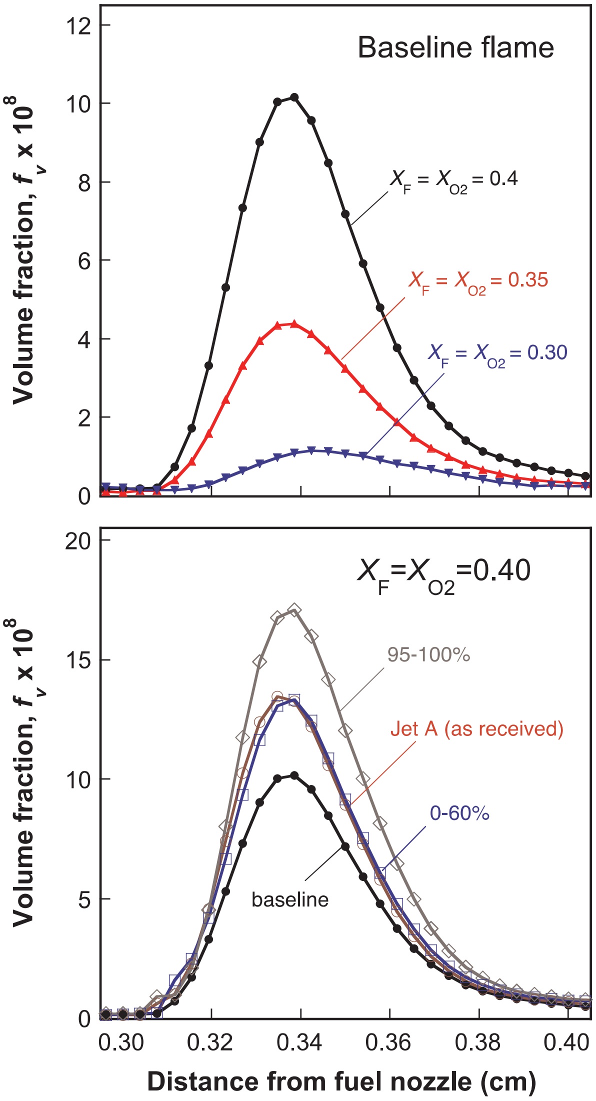

Fig. 10. Soot volume fraction profiles along the centerline. Top panel: baseline, undoped flames; bottom panel: flames at $X_F = X_{O_2} = 0.40$ doped with Jet A as received (0–100%), and its 0–60% and 95–100% distillate fractions. Symbols are experimental data; lines are drawn to guide the eyes.

Calculating the primary particle number density from the measured soot volume fraction and primary particle diameter reveals that the flame doped with the 95–100% distillate fraction generally has a higher particle number density at the height of maximum f_v, while those of the jet fuel as received and its 0–60% fraction are similar (see, Fig. S6 of the Supplementary Materials).

Fig. 13 shows the evolution of radial f_v profiles at three characteristic flame heights. Radially, the peak soot appears in the wings at HAB = 4.5 ± 0.1 cm, or 1.0 cm below the height at which the centerline soot f_v peaks. The peak soot volume fraction in the wings migrates and converges toward the centerline as HAB increases. The centerline f_v peaks at around 5.5 cm for all doped flames (the middle panel of Fig. 13), and eventually decreases in the peak value and more notably, in the wings (*cf*, the middle and top panels of Fig. 13). Again, in all cases, the effect of the distillate fraction on soot production is consistently observed, from the wings to the centerline of the flame, but like the counterflow diffusion flames tested, the effect is not as significant as one would observe in the premixed stretch-stabilized flames. Moreover since soot volume fraction is less than 2 ppm, the aggregate concentration is expected to be low, and the shielding and bridging effects can be neglected.

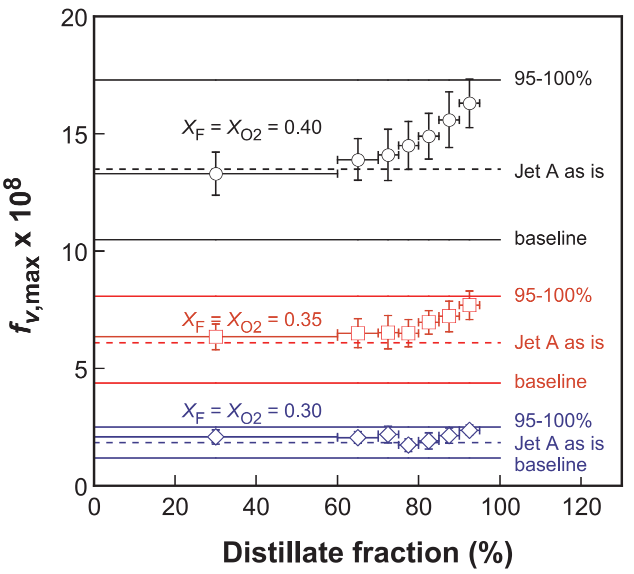

Fig. 11. Variation of the maximum soot volume fractions measured for different distillation fractions in three baseline flames. The horizontal lines mark the maximum volume fractions of the baseline flame, with additions of Jet A as received and the 95–100% fraction. The *x*-axis data value represents the center point of the distillate volume fraction range; its horizontal "error" bar represents the range of the respective distillate volume fraction.

4. Discussion

Aside from the fact that the data presented above are useful to the rational development of a reaction model for soot formation, there are several important findings that we can summarize concerning the sooting processes of real jet fuel. To start, evidence from literature [9–11] and the current study in premixed flames all suggest that one or more two-ring aromatic compounds must be considered in a fuel surrogate for it to reproduce the sooting properties. The results of the current study firmly attribute this to the presence of two-ring aromatic compounds in the tail end of the distillation curve. This evidence suggests that matching the sooting properties in any laboratory flames in which the liquid fuel is pre-vaporized may not truthfully mimic the real combustion situation in which the fuel is injected into a combustor as a spray. Preferential vaporization according to the different boiling points of fuel components can lead to the formation of pockets rich in high-molecular weight, multi-ring species.

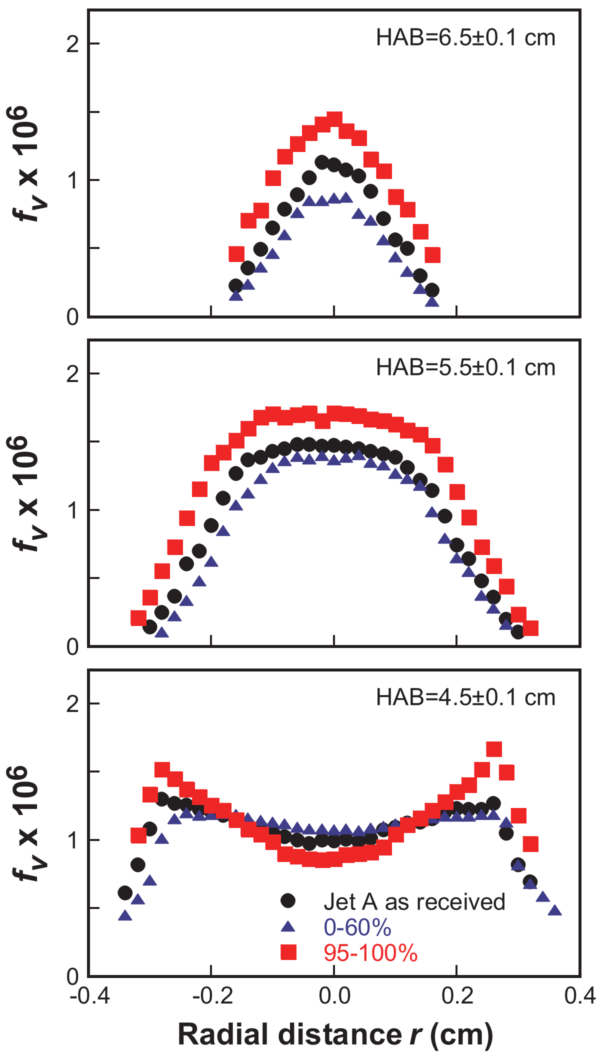

Fig. 13. Radial soot volume fraction profiles measured at three characteristic flame heights. HAB = 5.5 ± 0.1 cm corresponds to the maximum centerline volume fraction for each of the flames. The error bars are smaller than the symbols.

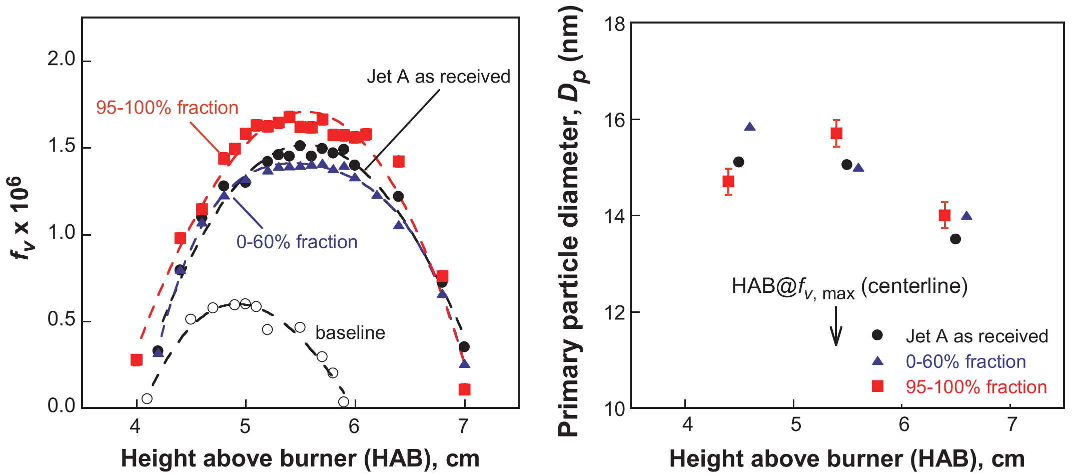

Fig. 12. Centerline soot volume fraction (left panel) and the particle diameter of primary particles (right panel) measured along the centerline of the coflow diffusion flame. Symbols are experimental data. Lines in the left panel are drawn to guide the eyes. The error bars represent one standard deviation of the sample size of around 500 counts. The error bars are discussed in section 2.4 and for the volume fraction they are smaller than the symbols.

The fuel components in the tail end of the distillation curve impact soot formation primarily through enhanced particle nucleation, as evidenced by the observations made in the premixed stretch-stabilized flames. For flames in which the soot yield is not as sensitive to nucleation, such as the counterflow and coflow diffusion flames studied herein, this effect is insignificant. Yet, the observation that soot formation can be sensitive to the distillation fraction poses another challenge in modeling soot formation in real fuels. Currently, it is unclear whether this effect must be accounted for in modeling soot formation in real engines. Suffice it to note that the surrogate fuel approach cannot account for the impact of preferential evaporation and its effect on soot formation and simultaneously make useful predictions for the heat release and flame extinction.

One of the interesting implications of the present findings is that to reduce soot production from real jet fuels, perhaps the most efficient approach is to place tighter constraints on the distillation process. As seen in Fig. 6, the temperature of the distillation curve shoots up above 90% of the volume fraction. It is in this fraction we expect to see drastically increased presence of multi-ring compounds. Excluding these compounds by keeping the upper limit of the distillation temperature to 250 °C would remove a large fraction of the multi-ring aromatic compounds and thus lowering the fuel sooting propensity. Of course, whether such a change can be made in the petroleum refining process, the cost associated with it and possible changes in other fuel properties remain to be open questions.

Lastly, we note that flames directly burning a certain distillate fraction would give a more direct measure for the distillate fraction dependent sooting property. Such experiments are more difficult, however, because the need for a large amount of fuel and the difficulties associated with the vaporization of high boiling point fractions in the experiment. We believe that the use of the distillate fraction in ethylene is as close to the real engine combustion condition as any lab experiments can get close to. The principle reason is that in the flame front jet fuels decompose to mainly ethylene [2,38], and as such the high-molecular weight fraction of the fuel mixed with ethylene does mimic the mixture properties under real combustion situation to a large extent. In any case, the mixture conditions in the flames probed here are much closer to those in real engines than sooting property experiments in which methane is used as the base fuel. In that case, the overall H/C ratio and hence the thermodynamic and chemical kinetic conditions are far different from those in engines.

5. Conclusions

The sooting properties of a typical Jet A (POSF 10325) were studied in detail across three flame platforms: the premixed stretch-stabilized flame, and counterflow and coflow diffusion flames, with an emphasis on the role of different distillate fraction of the fuel in soot formation. In all cases studied, the jet fuel or one of its distillate fractions is doped into baseline flames burning ethylene. The particle size distribution functions were also collected for the 2nd generation MURI surrogate in the premixed stretch-stabilized flame under comparable conditions. The results indicate:

1) The 2nd generation MURI surrogate does not reproduce soot nucleation in the premixed stretch-stabilized flame well. The cause is likely to be the lack of a two-ring compound in its formulation;
2) The tail end of the Jet A distillation curve is accompanied with an increased level of two-ring aromatic compounds (e.g., alkylated naphthalenes, alkylated biphenyls, and fluorenes), which drastically promote soot nucleation in the premixed stretch-stabilized flames;
3) In the diffusion flames studied, however, the effect just discussed is minor as soot production in these flames is more sensitive to soot surface growth than particle nucleation.

Taken together, the experimental measurements discussed herein are expected to be useful in formulating a rational strategy for modeling soot formation from real jet fuels. Such a strategy may have to consider the role of fuel evaporation as a necessary component of a predictive soot model.

Acknowledgements

The work at Stanford was supported by the National Aeronautics and Space Administration (NASA grant number NNX15AV05A). MRK was supported by NSERC Michael Smith Foreign Study award as well as BioFuelNet Canada exchange fund during his time at Stanford. Work at the University of Toronto was supported by NSERC and BioFuelNet Canada.

Appendix A. Supplementary data

Supplementary data associated with this article can be found, in the online version, at https://doi.org/10.1016/j.fuel.2018.07.099.

References

[1] Colket M, Heyne J, Rumizen M, Gupta M, Edwards T, Roquemore WM, et al. Overview of the National Jet Fuels Combustion Program. AIAA J 2017;55:1087–104.
[2] Xu R, Wang K, Banerjee S, Shao J, Parise T, Zhu Y, et al. A physics-based approach to modeling real-fuel combustion chemistry – II. Reaction kinetic models of jet and rocket fuels. Combust Flame 2018;193:520–37.
[3] Council CR. Handbook of aviation fuel properties. The Council 1983.
[4] Lovestead TM, Burger JL, Schneider N, Bruno TJ. Comprehensive assessment of composition and thermochemical variability by high resolution GC/QToF-MS and the advanced distillation-curve method as a basis of comparison for reference fuel development. Energy Fuels 2016;30(12):10029–44.
[5] Smith BL, Bruno TJ. TJ. Improvements in the measurement of distillation curves. 4. Application to the aviation turbine fuel Jet-A. Ind Eng Chem Res 2007;46(1):310–20.
[6] Burger JL, Bruno TJ. Application of the advanced distillation curve method to the variability of jet fuels. Energy Fuels 2012;26(6):3661–71.
[7] Moss J, Aksit I. Modelling soot formation in a laminar diffusion flame burning a surrogate kerosene fuel. Proc Combust Inst 2007;31(2):3139–46.
[8] Saffaripour M, Zabeti P, Kholghy M, Thomson MJ. An experimental comparison of the sooting behavior of synthetic jet fuels. Energy Fuels 2011;25(12):5584–93.
[9] Saffaripour M, Kholghy M, Dworkin S, Thomson MJ. A numerical and experimental study of soot formation in a laminar coflow diffusion flame of a jet A-1 surrogate. Proc Combust Inst 2013;34(1):1057–65.
[10] Saffaripour M, Veshkini A, Kholghy M, Thomson MJ. Experimental investigation and detailed modeling of soot aggregate formation and size distribution in laminar coflow diffusion flames of Jet A-1, a synthetic kerosene, and n-decane. Combust Flame 2014;161(3):848–63.
[11] Witkowski D, Kondo K, Vishwanathan G, Rothamer D. Evaluation of the sooting properties of real fuels and their commonly used surrogates in a laminar co-flow diffusion flame. Combust Flame 2013;160(6):1129–41.
[12] Aksit I, Moss J. Model fuels to reproduce the sooting behaviour of aviation kerosene. Fuel 2005;84(2–3):239–45.
[13] Mouis AG, Litzinger TA, Wang Y, Iyer V, Iyer S, Linevsky M, et al. Effects of a JP-8 surrogate and its components on soot in laminar, N 2-diluted ethylene co-flow diffusion flames from 1 to 5atm. Combust Flame 2015;162(5):1987–95.
[14] Jahangirian S, McEnally CS, Gomez A. Experimental study of ethylene counterflow diffusion flames perturbed by trace amounts of jet fuel and jet fuel surrogates under incipiently sooting conditions. Combust Flame 2009;156(9):1799–809.
[15] Bufferand H, Tosatto L, La Mantia B, Smooke M, Gomez A. Experimental and computational study of methane counterflow diffusion flames perturbed by trace amounts of either jet fuel or a 6-component surrogate under non-sooting conditions. Combust Flame 2009;156(8):1594–603.
[16] Tosatto L, La Mantia B, Bufferand H, Duchaine P, Gomez A. Chemical structure of a methane counterflow diffusion flame perturbed with the addition of either JP-8 or a jet fuel surrogate. Proc Combust Inst 2009;32(1):1319–26.
[17] Honnet S, Seshadri K, Niemann U, Peters N. A surrogate fuel for kerosene. Proc Combust Inst 2009;32(1):485–92.
[18] Carbone F, Gomez A. Chemical interactions between 1, 2, 4-trimethylbenzene and n-decane in doped counterflow gaseous diffusion flames. Proc Combust Inst 2015;35(1):761–9.
[19] Dagaut P, Gaïl S. Chemical kinetic study of the effect of a biofuel additive on Jet-A1 combustion. J Phys Chem A 2007;111(19):3992–4000.
[20] Dooley S, Won SH, Chaos M, Heyne J, Ju Y, Dryer FL, et al. A jet fuel surrogate formulated by real fuel properties. Combust Flame 2010;157(12):2333–9.
[21] Lemaire R, Therssen E, Pauwels J, Desgroux P. Experimental comparison of soot formation in turbulent flames of kerosene and surrogate model fuels. In: Bockhorn H, D'Anna A, Sarofim A, Wang H, eds. Combustion generated fine carbonaceous particles: proceedings of an international workshop held in Villa Orlandi, Anacapri.

Karlsruhe: KIT Scientific Publishing; 2009, p. 619–36.

[22] Dryer FL. Chemical kinetic and combustion characteristics of transportation fuels. Proc Combust Inst 2015;35(1):117–44.

[23] Dooley S, Won SH, Heyne J, Farouk TI, Ju Y, Dryer FL, et al. The experimental evaluation of a methodology for surrogate fuel formulation to emulate gas phase combustion kinetic phenomena. Combust Flame 2012;159(4):1444–66.

[24] Yang Y, Boehman AL, Santoro RJ. A study of jet fuel sooting tendency using the threshold sooting index (TSI) model. Combust Flame 2007;149(1–2):191–205.

[25] Das DD, McEnally CS, Kwan TA, Zimmerman JB, Cannella WJ, Mueller CJ, et al. Sooting tendencies of diesel fuels, jet fuels, and their surrogates in diffusion flames. Fuel 2017;197:445–58.

[26] Smith BL, Ott LS, Bruno TJ. Composition-explicit distillation curves of commercial biodiesel fuels: comparison of petroleum-derived fuel with B20 and B100. Ind Eng Chem Res 2008;47(16):5832–40.

[27] Commodo M, Wong O, Fabris I, Groth CP, Gülder ÖL. Spectroscopic study of aviation jet fuel thermal oxidative stability. Energy Fuels 2010;24(12):6437–41.

[28] Camacho J, Singh AV, Wang W, Shan R, Yapp EK, Chen D, et al. Soot particle size distributions in premixed stretch-stabilized flat ethylene–oxyge flames. Proc Combust Inst 2017;36(1):1001–9.

[29] Camacho J, Liu C, Gu C, Lin H, Huang Z, Tang Q, et al. Mobility size and mass of nascent soot particles in a benchmark premixed ethylene flame. Combust Flame 2015;162(10):3810–22.

[30] Abid AD, Camacho J, Sheen DA, Wang H. Quantitative measurement of soot particle size distribution in premixed flames–the burner-stabilized stagnation flame approach. Combust Flame 2009;156(10):1862–70.

[31] Li Z, Wang H. Drag force, diffusion coefficient, and electric mobility of small particles. I. Theory applicable to the free-molecule regime. Phys Rev E 2003;68(6):061206.

[32] Singh J, Patterson RI, Kraft M, Wang H. Numerical simulation and sensitivity analysis of detailed soot particle size distribution in laminar premixed ethylene flames. Combust Flame 2006;145(1–2):117–27.

[33] Li Z, Wang H. Drag force, diffusion coefficient, and electric mobility of small particles. II. Application. Phys Rev E 2003;68(6):061207.

[34] Li Z, Wang H. Comment on “Phenomenological description of mobility of nm-and sub-nm-sized charged aerosol particles in electric field” by Shandakov, SD, Nasibulin, AG and Kauppinen, EI. J Aerosol Sci 2006;37(1):111–4.

[35] Wang H. Formation of nascent soot and other condensed-phase materials in flames. Proc Combust Inst 2011;33:41–67.

[36] Banerjee S, Tangko R, Sheen DA, Wang H, Bowman CT. An experimental and kinetic modeling study of n-dodecane pyrolysis and oxidation. Combust Flame 2016;163:12–30.

[37] Cuoci A, Frassoldati A, Faravelli T, Ranzi E. OpenSMOKE++: An object-oriented framework for the numerical modeling of reactive systems with detailed kinetic mechanisms. Comput Phys Commun 2015;192:237–64.

[38] Wang H, Xu R, Wang K, Bowman CT, Davidson DF, Hanson RK, et al. A physics-based approach to modeling real-fuel combustion chemistry – I. Evidence from experiments, and thermodynamic, chemical kinetic and statistical considerations. Combust Flame 2018;193:502–19.

[39] Singh P, Hui X, Sung C-J. Soot formation in non-premixed counterflow flames of butane and butanol isomers. Combust Flame 2016;164:167–82.

[40] Singh P, Sung C-J. PAH formation in counterflow non-premixed flames of butane and butanol isomers. Combust Flame 2016;170:91–110.

[41] Xue X, Hui X, Singh P, Sung C-J. Soot formation in non-premixed counterflow flames of conventional and alternative jet fuels. Fuel 2017;210:343–51.

[42] Shaddix CR, Smyth KC. Laser-induced incandescence measurements of soot production in steady and flickering methane, propane, and ethylene diffusion flames. Combust Flame 1996;107(4):418–52.

[43] Kholghy M, Afarin Y, Sediako AD, Barba J, Lapuerta M, Chu C, et al. Comparison of multiple diagnostic techniques to study soot formation and morphology in a diffusion flame. Combust Flame 2017;176:567–83.

[44] Snelling DR, Thomson KA, Smallwood GJ, Gülder ÖL, Weckman E, Fraser R. Spectrally resolved measurement of flame radiation to determine soot temperature and concentration. AIAA J 2002;40(9):1789–95.

[45] Nestor O, Olsen H. Numerical methods for reducing line and surface probe data. SIAM Rev 1960;2(3):200–7.

[46] Thomson KA. Soot formation in annular non-premixed laminar flames of methane-air at pressures of 0.1 to 4.0 MPa. University of Waterloo; 2004.

[47] Williams TC, Shaddix C, Jensen K, Suo-Anttila J. Measurement of the dimensionless extinction coefficient of soot within laminar diffusion flames. Int J Heat Mass Tran 2007;50(7–8):1616–30.

[48] Snelling DR, Liu F, Smallwood GJ, Gülder ÖL. Evaluation of the nanoscale heat and mass transfer model of LII: prediction of the excitation intensity. In: Proceedings of the 34th national heat transfer conference. 2000, p. 79–87.

[49] Snelling DR, Liu F, Smallwood GJ, Gülder ÖL. Determination of the soot absorption function and thermal accommodation coefficient using low-fluence LII in a laminar coflow ethylene diffusion flame. Combust Flame 2004;136(1–2):180–90.

[50] Saffaripour M, Geigle K-P, Snelling D, Smallwood G, Thomson K. Influence of rapid laser heating on the optical properties of in-flame soot. Appl Phys B-Lasers O 2015;119(4):621–42.

[51] Bachalo WD, Sankar SV, Smallwood GJ, Snelling DR. Development of the laser-induced incandescence method for the reliable characterization of particulate emissions. In: 11th international symposium on applications of laser techniques to fluid mechanics. Lisbon, Portugal; July, 2002, p. 8–111.

[52] Schenk M, Lieb S, Vieker H, Beyer A, Gölzhäuser A, Wang H, et al. Imaging nanocarbon materials: soot particles in flames are not structurally homogeneous. ChemPhysChem 2013;14(14):3248–54.

[53] Schenk M, Lieb S, Vieker H, Beyer A, Gölzhäuser A, Wang H, et al. Morphology of nascent soot in ethylene flames. Proc Combust Inst 2015;35(2):1879–86.

[54] Das DD, Cannella WJ, McEnally CS, Mueller CJ, Pfefferle LD. Two-dimensional soot volume fraction measurements in flames doped with large hydrocarbons. Proc Combust Inst 2017;36(1):871–9.

[55] Zhang T, Zhao L, Kholghy M, Thion S, Thomson MJ. Detailed investigation of soot formation from jet fuel in a diffusion flame with comprehensive and hybrid chemical mechanisms. Proc Combust Inst 2019:accepted.

[56] Hura HS, Glassman I. Soot formation in diffusion flames of fuel/oxygen mixtures. Symp (Int) Combust 1989;22(1):371–8.

[57] Zhang T, Thomson MJ. A numerical study of the effects of n-propylbenzene addition to n-dodecane on soot formation in a laminar coflow diffusion flame. Combust Flame 2018;190:416–31.

[58] Zhang T, Zhao L, Thomson MJ. Effects of n-propylbenzene addition to n-dodecane on soot formation and aggregate structure in a laminar coflow diffusion flame. Proc Combust Inst 2017;36(1):1339–47.